The Atmospheric Boundary Layer during Swell: A Field Study and Interpretation of the Turbulent Kinetic Energy Budget for High Wave Ages

U. HÖGSTRÖM, A. SMEDMAN, AND E. SAHLEÉ

Department of Earth Sciences, Uppsala University, Uppsala, Sweden

W. M. DRENNAN

Rosenstiel School of Marine and Atmospheric Science, University of Miami, Miami, Florida

K. K. KAHMA AND H. PETTERSSON

Finnish Institute of Marine Research, Helsinki, Finland

F. ZHANG

Rosenstiel School of Marine and Atmospheric Science, University of Miami, Miami, Florida

ABSTRACT

Analysis of the turbulent kinetic energy (TKE) budget for five slightly unstable cases with swell has been performed based on measurements of mechanical production, buoyancy production, turbulent transport, and dissipation at five levels over the sea, from 2.5 to 26 m. The time rate of change and advection of TKE were found to be small, so the TKE residual is interpreted as an estimate of the pressure transport term (T_p). In two cases with high wave age, the T_p term is a gain at all heights. For three cases with smaller wave age, T_p is a loss in the TKE budget below 5–10 m and a gain for greater heights, where the decrease is exponential, thus showing the combined effects of swell waves and a range of waves traveling slower than the wind. The TKE budget for a case with growing sea but similar wind speed and stability as some of the swell cases has T_p close to zero at all heights. It is shown that the observed characteristic wind profile with either a low-level maximum in the 5–10-m range or a distinct "knee" at that height is an effect of the T_p term.

1. Introduction

In Smedman et al. (2009, hereafter SH09) below, data from the Baltic Sea Swell Experiment (BASE) were used to study the characteristics of situations with swell, defined as $c_p/U_8 > 1.2$, where c_p is the phase velocity of the dominant swell waves and U_8 is the wind speed at 8 m. The measurements included data from an anchored Air–Sea Interaction Spar (ASIS) buoy and a nearby 30-m tower in the height range 2.5 to 30 m above the water. A particularly significant finding was a low-level wind maximum or a distinct "knee" in the wind profile—that is, an abrupt change from a layer with rapidly in-creasing wind with height in a layer near the water surface to a deep layer of virtually constant wind (extending to the top of the unstable boundary layer at 200 m during one day with balloon wind profile measurements). Such phenomena were observed in all swell cases (comprising 147 half-hour mean values) during the roughly 45-day measurement period. The wind maximum or the knee was observed at 5–10 m above the water surface. As discussed in SH09, previous observations of this phenomenon in marine conditions are rare, the main reason probably being that simultaneous observations of wind profiles extending all the way from a couple of meters to several tens of meters above the surface of the ocean are rare.

In SH09, observed characteristics (beside the mean wind profile) of the swell boundary layer include mean profiles of shearing stress and of along-wind and vertical velocity variances and of the *u–w* correlation. It was

Corresponding author address: Ulf Högström, Dept. of Earth Sciences, Uppsala University, Villavägen 16, Uppsala S-752 36, Sweden.
E-mail: ulf.hogstrom@met.uu.se

noted in SH09 that the atmospheric swell boundary layer has characteristics that differ significantly from nonswell boundary layers with similar 10-m wind speed, U_{10}, and Obukhov length, L. Thus, Monin–Obukhov similarity does not apply and the surface shearing stress is more or less strongly suppressed. The observed features were compared with results from the large-eddy simulations (LES) by Sullivan et al. (2004, 2008), and good qualitative agreement was observed with the corresponding results for their ''wind-following swell case with light convection.'' This agreement was considered to be particularly remarkable in view of the great disparity in wave slope: in the LES, the wave slope was 0.1, in contrast with our values between 0.015 and 0.029. A similar result was also obtained from the simple 1D simulations of Hanley and Belcher (2008). An interesting result of our study was the lack of sensitivity of the results to the value of the angle between the swell and the wind in the range 0° to 90°.

No attempt was made in SH09 to explain the observed features. This is the purpose of the present paper. The starting point is the fact that the surface form stress must be the key factor, as illustrated in the LES study of Sullivan et al. (2008). During swell it produces a forward thrust on the flow (which is balanced by the pressure gradient force by a slight turning of the wind compared to the nonswell case). This positive form stress is transferred to higher levels in the atmospheric boundary layer by the pressure transport term, which can, in principle, be obtained as a residual in the turbulent kinetic energy (TKE) budget, provided the individual terms are determined with sufficient accuracy. A problem arises, however, for cases in which the wind is not very low as a result of smaller-scale waves that are also present at the surface of the ocean, riding on top of the long swell waves and producing a negative form stress at the surface. Provided there is enough energy in the appropriate wavelength band (see below), this may lead to a negative contribution to the pressure transport term in the layer below the wind maximum or knee. Thus, for these cases, the observed pressure transport term is expected to be the sum of the positive contribution from swell and a negative contribution from shorter waves.

Section 2 gives a brief account of the experimental data, section 3 provides the basic theoretical background, and sections 4, 5, and 6 contain results, discussion, and conclusions, respectively.

2. Experimental data

A detailed account of the measurements is given in Högström et al. (2008) and in SH09. Here only a short summary of relevant information is given.

BASE took place during September–October 2003 around the Uppsala University Östergarnsholm field station in the Baltic Sea. Turbulence measurements were made with Gill R2/R2A sonic anemometers at five levels, two of which are from an ASIS buoy (Graber et al. 2000), 2.5 and 5.3 m above mean water level, and the remaining three from the Östergarnsholm tower, at nominal heights 10, 18, and 26 m above the water surface. ASIS was moored in 30 m of water about 4 km southeast of the tower, in the upwind direction for the measurements discussed here. These measurements provide most of the data needed for the analysis of the TKE budget, but mean wind profile data are also required. Such measurements were made at 1.18 (only for a limited period of time), 2.4, and 5.3 m on ASIS and at the following heights on the tower: 8, 13, 16, 22, and 30 m above mean sea level. Additional measurements, including surface waves and sea surface temperature, were made from ASIS and from two directional Waverider buoys moored in the area. Directional wave analysis followed the description of Pettersson et al. (2003).

In SH09 detailed analysis was performed for five selected cases with swell: C1, C2, and C3, which all have wind direction roughly perpendicular to the swell propagation direction, and wave age c_p/U_8 equal to 4.7, 1.79, and 1.61, respectively; cases F1 and F2 have a wind–wave angle close to zero and c_p/U_8 equal to 4.6 and 1.73, respectively. Each case is formed as a mean of data from 5 to 19 half-hour periods. The TKE analyses presented here have been carried out for the same five cases.

3. Basic theoretical considerations

The form stress or pressure drag over a wave with wavelength λ is obtained from

$$(D_p)_0 = \frac{1}{\lambda} \int_0^\lambda p \frac{d\eta}{dx} dx, \qquad (1)$$

where η is the height of the wave surface at position x and p is the pressure on the surface at x. By writing

$$\frac{d\eta}{dx} = \frac{d\eta}{dt} \frac{dt}{dx} = \tilde{w} \frac{1}{c}, \qquad (2)$$

where $\tilde{w}$ is the vertical velocity at the surface and $c =$ the wave phase speed, Eq. (1) can be written

$$(D_p)_0 = \frac{1}{\lambda} \frac{1}{c} \int_0^\lambda (\tilde{p}\tilde{w}) dx = \frac{\langle \tilde{p}\tilde{w} \rangle}{c}, \qquad (3)$$

where $\tilde{p}$ is the pressure at the wavy surface and $\langle \ \rangle$ denotes an average over one wavelength.

A necessary requirement for $(D_p)_0 \neq 0$ is that there is a phase shift between $\tilde{p}$ and η that differs from 180°. The LES of Sullivan et al. (2008) shows that in the case of swell waves aligned with and leading the wind, "the negative pressure pattern is shifted slightly behind the wave crest hence the integration of the surface pressure over the wave acts in the positive x direction implying a thrust on the winds." From analysis of the results presented in Sullivan et al. (2008), it can be concluded that the phase shift is less than 180° and only of the order 2°. For waves traveling slower than the wind (i.e., for normal wind seas), the pressure pattern is shifted slightly ahead of the wave crest (phase shift over 180°) producing the opposite sign of the pressure drag, called $(D_{sf})_0$ below, and resulting in growth of the waves.

The pressure stress created at the surface of the ocean must be transferred to the overlying atmosphere. The few existing pressure fluctuation measurements (e.g., Elliot 1972; Donelan et al. 2006) support the results derived from potential flow theory that wave-induced pressure fluctuations decay as e^{-kz}, where k is wavenumber = $2\pi/\lambda$. Figure 13 in Sullivan et al. (2008) shows that when the waves are moving, the variance of the vertical velocity decays with height approximately exponentially. The Sullivan et al. (2008) model resolves only the large-scale fluctuations, which near the surface are dominated by wave-correlated velocities. Because of that, the pressure stress,

$$D_p(z) = \frac{\overline{p'(z)w'(z)'}}{c}, \qquad (4)$$

will decay exponentially with height and at a faster rate than e^{-kz} in the model results. The decay rate can be estimated from Fig. 12 of Sullivan et al. (2008). It shows the LES of normalized pressure stress as a function of normalized height, z/z_i, where z_i is the height of the boundary layer, for several situations. We have selected their curve for "slight convection with waves traveling with and faster than the wind" and replotted the result (values for normalized pressure stress extracted manually from their plot for five equidistant values of normalized height) in a linear–logarithmic representation (Fig. 1). The data are indeed well described by a straight line in this representation, implying that

$$D_p = A_0 e^{-B_0 kz}, \qquad (5)$$

where A_0 and B_0 are parameters to be determined, with A_0 being equal to the form stress, $(D_p)_0$ defined by Eq. (1).

The parameter B_o can be determined from the slope of the line in Fig. 1 provided the wavelength λ and
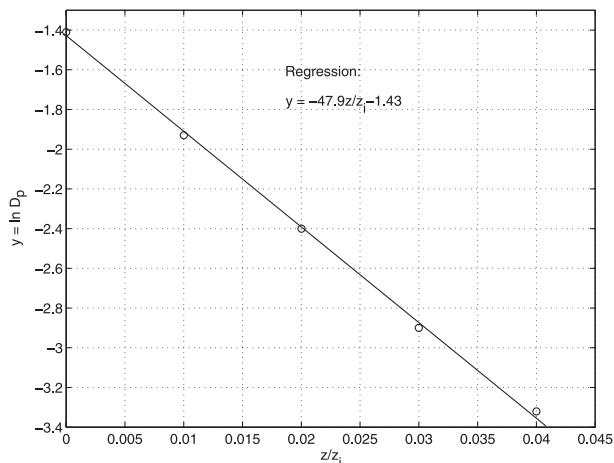
FIG. 1. Vertical profiles of the natural logarithm of normalized pressure stress, D_p, obtained from large-eddy simulations by Sullivan et al. (2008) for the case of "slight convection with waves traveling with and faster than the wind" plotted against z/z_i, where z is the height above the water surface and z_i is the height of the boundary layer, here 400 m. The simulation is based on a monochromatic wave with $\lambda = 100$ m. The circles are data extracted manually from Fig. 12 of Sullivan et al. (2008). [Adapted from Sullivan et al. (2008).]

the boundary layer height z_i are known. According to Sullivan et al. (2008), the following parameter values were used in the LES: $\lambda = 100$ m and $z_i = 400$ m. With these parameter values and the slope of the regression line, −47.9, it is concluded that $B_o \approx 1.9$. The variance of the vertical velocity does not behave in our data as it does in the Sullivan et al. (2008) model, but because our data also contain the small-scale fluctuations, this does not imply that 1.9 would not apply to our data also. We will therefore use $B_o \approx 1.9$ as an ad hoc assumption in the analysis of our data. Below, the pressure transport term is evaluated as a residual from the measurements of the remaining terms of the TKE budget, so in principle it would be possible to evaluate the parameter B_o, but the uncertainty of the individual estimates of the present data is such that this is not possible in practice. In fact, the analysis described below, which assumes $B_o = 1.9$, was also made with $B_o = 1.0$ (not shown). The details of the results of this study were of course different from the present, but the general results were essentially the same. Thus, the numerical results must be regarded as only semiquantitative. It is tempting to make use of critical-layer theory (Miles 1957), which builds on the concept of resonant wind–wave interaction. From this theory it follows that there is a particular critical height z_{cr}, for each wave mode, defined by the phase speed of that mode, c, and the relation

$$c = U(z_{cr}), \qquad (6)$$

where $U(z)$ is mean wind speed. Hristov et al. (2003) used a linear filter (Hristov et al. 1998) to identify the wave-induced airflow from measurements at the platform R/P *FLIP* during oceanic conditions and found very good quantitative agreement with the phase shift of filtered w predicted by the critical-layer theory. This theory is, however, still controversial. As pointed out by a reviewer, a requirement for the theory to hold is curvature in the wind profile. This is not valid for our swell cases for the approximate height interval 2.5–8 m, where the wind profiles are found to be close to linear (cf. Figs. 3a,b of SH09). From Eq. (5), however, it is evident that the pressure stress induced by the waves is strongly wavenumber dependent. This means that short waves can exert significant pressure stress influence to much lower height than long swell waves. This is the important point in the discussion to follow. Instead of the term critical height we will use the looser term "height of influence," z_w.

As will be discussed in detail later, the height of influence for the short waves is expected to be less than about 8 m (the height of the knee in the wind profiles for cases C2, C3, and F2). Returning for the moment to the terminology of critical height, the simulations shown in Hristov et al. (2003, their Fig. 1) indicate a very complicated pattern for the region close to z_{cr}. Thus, for the height range involved, $0 < z < 8$ m, $z/z_{cr} \approx z/z_w$ is not so small that we may expect Eq. (5) to be valid.

4. Results

a. Determination of the terms of the turbulence kinetic energy budget

The turbulent kinetic energy budget for the general case reads

$$\underbrace{\frac{\partial \overline{q'^2}}{2\partial t}}_{\text{Trc}} + \underbrace{\overline{\mathbf{U} \cdot \mathbf{\nabla}\left(\frac{q'^2}{2}\right)}}_{\text{Adv}} = \underbrace{\overline{u'w'}\frac{\partial \overline{U}}{\partial z}}_{P} - \underbrace{\frac{g}{T}\overline{w'\theta'_v}}_{B} + \underbrace{\frac{\partial}{\partial z}\frac{\overline{wq'^2}}{2}}_{T_t}$$
$$+ \underbrace{\frac{1}{\rho}\frac{\partial \overline{p'w'}}{\partial z}}_{T_p} + \varepsilon \qquad (7)$$

Here, $q'^2/2$ is the instantaneous TKE = ½($u'^2 + v'^2 + w'^2$), where u', v', and w' are instantaneous deviations of, respectively, the longitudinal, lateral, and vertical wind components from their respective mean values; $\mathbf{U}$ is the horizontal wind vector; $\overline{U}$ is the magnitude of the mean wind, which varies with height z; g is acceleration of gravity; T is mean temperature of the surface layer in kelvins; θ_v is the instantaneous deviation of virtual temperature from its mean; ρ is air density; p is

instantaneous deviation of air pressure; and ε is dissipation of TKE. The overbars represent averages (in the present study, a time average over 30 min). The same five swell cases that were selected for analysis in the companion paper SH09 and, as a reference, one growing sea case will be analyzed, each case being the mean of 5–19 half-hour periods (see Table 1 of SH09). That is, each of the terms in (7) is evaluated separately for every half-hour period and then a case average is derived.

The physical interpretation of the seven terms in (7) is as follows: Trc = local time rate of change of TKE; Adv = advection by the mean wind of TKE; P = shear production of TKE; B = buoyancy production; T_t = vertical divergence of the turbulent transport of TKE; T_p = vertical divergence of the pressure transport of TKE; and ε = dissipation of TKE. The analysis of measured data (see the appendix) shows that the Trc and Adv terms are generally much smaller than the dominating terms on the right-hand side of the equation.

All terms except T_p can be evaluated directly from the simultaneous turbulence measurements at two levels on ASIS, 2.5 and 5.3 m above mean water level, and three levels on the tower, 10, 18, and 26 m (see SH09 for details). In addition, for the derivation of the term P, mean wind data from seven levels are required. The remaining term, T_p, is derived as a residual. The evaluation procedures adopted for the terms P, B, T_t, and ε are briefly outlined below. For an in-depth analysis, see the appendix, where the procedures for the evaluation of mean values of each term are given together with the derivation of error estimates.

1) Turbulence production:

$$P = \overline{u'w'}\frac{\partial U}{\partial z}. \qquad (8)$$

This term is evaluated from measurements of the shearing stress $\overline{u'w'}$ and the mean wind gradient at each turbulence level (2.5, 5.3, 10, 18, and 26 m, approximately).

2) The buoyancy term:

$$B = -\frac{g}{T}\overline{w'\theta'_v}. \qquad (9)$$

This term requires only the "raw" measurements of turbulent flux of virtual temperature, which is very nearly equal to the corresponding flux of "sonic" temperature, obtained directly from the sonic measurements at each turbulence level, and estimates of the mean temperature at each level.

3) The turbulent transport term T_t can be written

$$T_t = \frac{1}{2}\frac{\partial}{\partial z}(\overline{w'u'^2} + \overline{w'v'^2} + \overline{w'^3}) = \frac{\partial \overline{w'E'}}{\partial z}. \qquad (10)$$

Each of the three third-order terms $\overline{w'u'^2}$, $\overline{w'v'^2}$, and $\overline{w'^3}$ are obtained from the turbulence measurements at the five turbulence levels and their sum is plotted against height. From this kind of plot (one for each case), graphic fits can be done from which estimates of vertical derivatives can be obtained (see the appendix) as well as error estimates.

4) Dissipation, ε.

Power spectra for the u component premultiplied by frequency $nS_u(n)$ were plotted on a log–log scale against frequency n for all five cases and heights (2.5, 5, 10, 18, and 26 m). According to Kolmogoroff (1941), and further assuming Taylor's hypothesis to be valid, the spectral curves in the inertial subrange are expected to be straight lines with $-2/3$ slope in this representation,

$$nS_u(n) = \alpha_1 \varepsilon^{2/3} \left(\frac{2\pi n}{U} \right)^{-2/3}, \qquad (11)$$

so that

$$\varepsilon = \frac{2\pi n}{U} \left[\frac{nS_u(n)}{\alpha_1} \right]^{3/2}, \qquad (12)$$

Here α_1 is a universal constant ≈ 0.50 (cf. Högström 1990) and n must be chosen in the region with $-2/3$ slope. Details of the evaluation and error analysis are given in the appendix.

5) The pressure transport term, T_p.

Because it was found (see the appendix) that the left-hand-side terms of Eq. (7) are much smaller than the right-hand-side terms (see below), the pressure transport T_p, can be calculated as the residual (i.e., as minus the sum of the terms P, B, T_t, and ε). The standard error of the mean for T_p is derived from the expression

$$\delta T_p = \sqrt{\delta P^2 + \delta B^2 + \delta T_t^2 + \delta \varepsilon^2}, \qquad (13)$$

where δT_p = standard error of the mean (s.e.m.) for T_p, δP = s.e.m. for P, etc.

For each of the five swell cases (C1, F1, C2, C3, F2) and the growing sea reference case, plots have been made (Figs. 2a–f) showing the variation with height of all the TKE budget terms, P, B, T_t, ε and T_p. Corresponding observations are circles, triangles, stars, squares, and filled circles connected with full lines. Also shown are hatched and dotted lines, which will be discussed below. Note that the TKE scale varies to a considerable degree between the cases, being less than $\pm 5 \times 10^{-4}$ m^2 s^{-3} for cases C1 and F1 (Figs. 2a,b)

and $\pm 8 \times 10^{-3}$ m^2 s^{-3} for case F2 (Fig. 2e). Also shown as insert figures in Figs. 2a–f are the mean wind profile for each particular case.

As discussed in detail in the appendix, all identified possible sources of error have been quantified and included in estimation of the resulting standard error of the mean for each of the terms P, B, T_t, and ε and are presented as error bars in the graphs for each case and height. The corresponding error bars for T_p were derived with Eq. (13). Generally speaking, some of the error bars are large (particularly so for T_p), but there are characteristic patterns that distinguish the TKE plots for the high–wave age cases C1 and F1 from the relatively low–wave age cases C2, C3, and F2. Thus, the TKE plots in Figs. 2a–f are, in a sense, only semiquantitative, but there are no reasons to expect them to be systematically biased.

b. TKE budgets for the five selected swell cases and the growing sea reference case

General features of the TKE plots for the swell cases are as follows: As expected from the wind profile shape (insert figures), the mechanical production term $-P$ either decreases rapidly with height up to about 8 m (cases C2, C3, and F2) or is close to zero everywhere (case C1 and F1, which have $\overline{u'w'} \approx 0$ at all heights), being close to zero higher up for all cases. The buoyancy production term B is virtually constant with height for all cases. The turbulent transport term T_t is a small loss, either height constant (cases C1 and F1) or decreasing with height. Dissipation ε is the dominant loss term, which decreases with height.

The pressure transport term T_p (strictly speaking, the residual) for the two cases with high wave age and low wind speed, C1 and F1, is clearly negative at all heights (except at 18 m for case C1, where it is slightly positive) and, considering the width of the corresponding error bars, it can easily be reconciled with a curve of the form ae^{-bz}, where a and b are constants. The dashed lines indicate three alternative such curves, which are forced to go through the observed value of T_p at 10 m, T_{pm}, and through $T_{pm} \pm$ s.e.m., respectively. Later, we will interpret these curves in terms of the theory outlined in section 3.

The T_p curves for the three remaining swell cases, C2, C3, and F2, behave distinctly differently from cases C1 and F1, being positive at low heights but changing sign slightly below 10 m, decreasing apparently asymptotically to zero with further increase in height.

In contrast to this persistent T_p pattern for the swell cases, Fig. 2f shows that T_p is very small for the growing sea case, being in fact within $\pm$s.e.m. of zero at all heights. This pattern suggests that the T_p curves
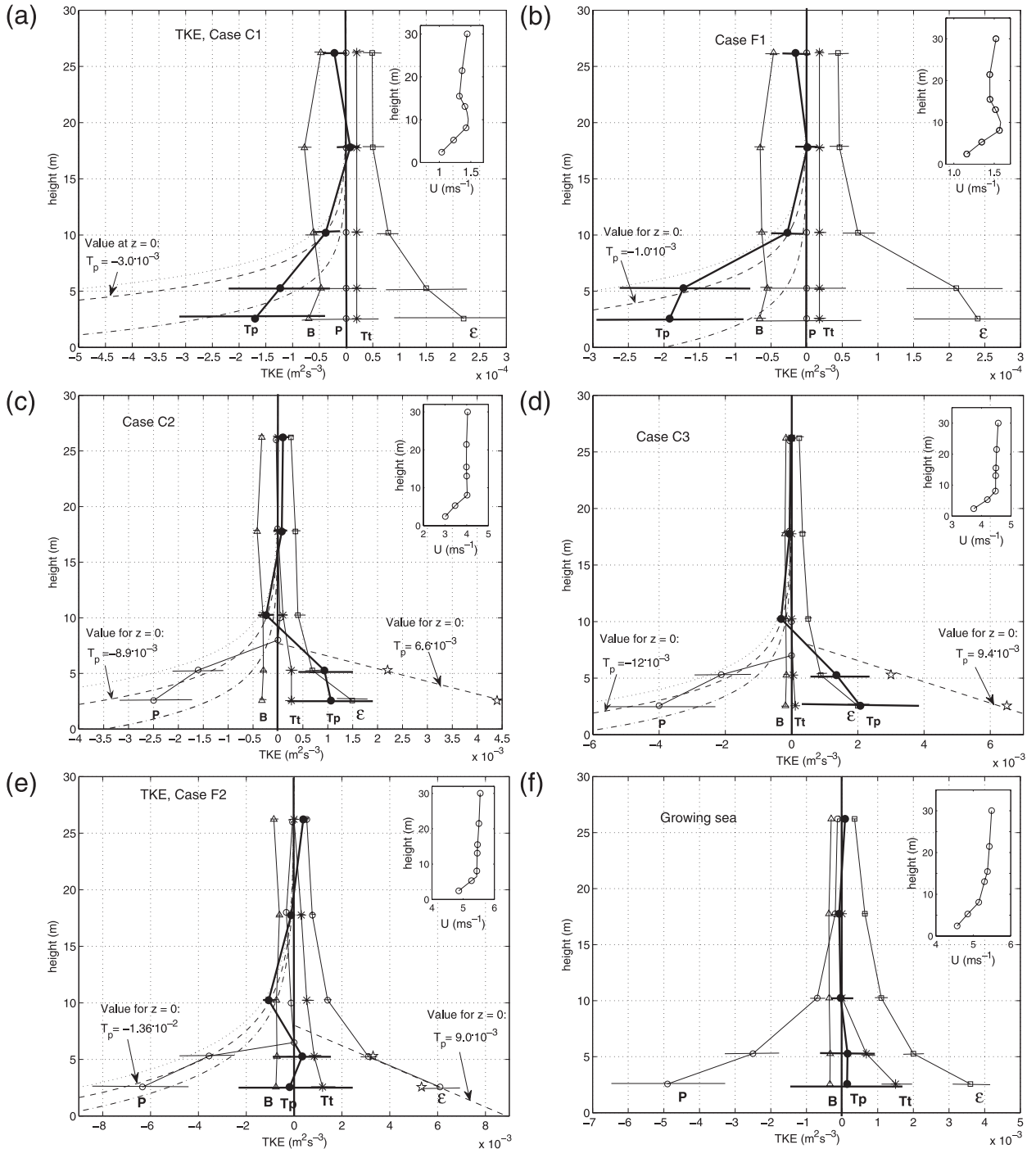
FIG. 2. TKE budgets for different cases, where open circles are measurements for P = mechanical production, triangles for B = buoyancy production, stars for T_t = turbulent transport, squares for ε = dissipation, and filled circles for T_p = pressure transport, which have all been connected with straight lines. Horizontal bars indicate ±standard error of the mean. Dashed lines indicate possible exponential functions for T_p (see text). Insert: the mean wind profile for the case. Cases (a) C1; (b) F1; (c) C2; (d) C3; (e) F2; and (f) for the growing sea case. In (c)–(e), open stars and dashed line indicate positive TKE (see text).

obtained for the swell cases may indeed be a signature of the effect of the wave field on the atmospheric TKE.

c. A model for analysis of the pressure transport mechanism

In SH09 it was observed that the wind profile has either a clear maximum (case C1 and F1) or a distinct knee (cases C2, C3, and F2) somewhere in the height range 5–10 m. From Eq. (5), it is reasonable to expect only waves with sufficiently small wavenumber k (i.e., swell waves) to influence the atmospheric boundary layer structure well above 10 m; for lower levels, effects from shorter waves riding on top of the swell waves may contribute. According to Eq. (5), it is predicted that the pressure stress from a monochromatic wave mode would vary exponentially with height. This expression, together with Eq. (4), enables an expression for the pressure transport term

$$T_p = \frac{1}{\rho} \frac{\partial \overline{p'w'}}{\partial z} = -A_0 B_0 k c \frac{1}{\rho} e^{-B_0 k z}, \qquad (14)$$

where it is further assumed (see section 3 and Sullivan et al. 2008) that $B_0 \approx 1.9$. Inserting observed values for the swell peak wavelength for cases C1 and F1 from Table 1 of SH09 in (14), the dashed curves in Figs. 2a,b are obtained. As noted previously, the curves are made to go through the observed mean value for T_p at 10 m, T_{pm}, and through $T_{pm} \pm$ s.e.m., respectively. The observed T_p curves with their respective error bars for these two cases are seen to support this model within the accuracy of the T_p estimates, in particular for case F1.

For cases C2, C3, and F2, we expect an influence of short waves near the surface. It is reasonable to assume that the height of influence for those waves $< z_{U\max}$ (i.e., the height of the knee in the respective wind profile); $z_{U\max}$ is around 7.5 m. For heights $\gtrsim 7.5$ m, it is assumed that the observed T_p curve reflects exclusively the effect of the swell waves, so that Eq. (14) with $B_0 \approx 1.9$ is valid.

For $z < 7.5$ m, we write formally

$$(T_p)_m = (T_p)_{\exp} + (T_p)_s, \qquad (15)$$

where $(T_p)_m$ is measured T_p, $(T_p)_{\exp}$ is derived from Eq. (14) for the case of the exponential curve going through the measured value at 10 m, and $(T_p)_s$ is the contribution to T_p from shorter waves. Thus, $(T_p)_s$ can be derived with Eq. (15) for the heights 2.5 and 5 m. In Figs. 2c,d,e they have been plotted with open star symbols. For each of the cases C2, C3, and F2, a straight line is an approximate fit for $(T_p)_s$:

$$(T_p)_s = C(7.5 - z), \quad z < 7.5 \text{ m}, \qquad (16)$$

where $C = d(T_p)_s / dz$, which is thus constant for each particular case.

Equation (16) has no theoretical backing, being just an approximate fit to the stars and the reasonable assumption that $(T_p)_s$ is zero near $z = 7.5$ m, which, as noted above, is the approximate height of the knee in the wind profiles. In fact, attempts to fit the observations with Eq. (14) and observed wavelengths do not give anything like acceptable results.

d. Interpretation of the results from the T_p analysis

In general, the drag at the surface, $\tau = -\rho u_{*0}^2$, is the sum of a tangential, or viscous, component, D_{visc}, and a form drag. The form drag has the same sign (minus) as the tangential drag for waves traveling slower than the wind, $(D_{sf})_0$, and the opposite sign (plus) for swell waves (i.e., waves traveling faster than the wind), $(D_p)_0$:

$$\tau = -\rho u_{*0}^2 = D_{\mathrm{visc}} + (D_{sf})_0 + (D_p)_0. \qquad (17)$$

For swell situations in general, the magnitude of $(D_p)_0$ may be greater than the magnitude of the sum $D_{\mathrm{visc}} + (D_{sf})_0$, so that τ is positive, implying that there is a net upward transport of momentum. Such situations have been observed over the ocean (e.g., Grachev and Fairall 2001; Smedman et al. 1994) and in the LES of Sullivan et al. (2004, 2008), but in our five swell cases, τ is either zero (cases C1 and F1) or negative.

For the swell form drag, we have, from Eq. (5),

$$(D_p)_0 = A_0. \qquad (18)$$

A rough estimate of the form drag of the short waves, $(D_{sf})_0$, can be obtained from the measurements, provided another assumption is made concerning the vertical velocity–pressure covariance resulting from the short waves, $(\overline{p'w'})_s$. Because the vertical derivative of that term is zero at around 7.5 m, it is reasonable to assume that $(\overline{p'w'})_s$ is also zero at 7.5 m (otherwise it would require a mechanism for it to survive to infinity without further attenuation, which is unlikely). From Eq. (16) and the relation $(D_{sf})_0 = (\overline{p'w'})_s / c_s$, where c_s is a wave phase speed characteristic of the short waves that contribute to the drag (cf. below), we get

$$(T_p)_s = C(7.5 - z) = \frac{1}{\rho} \frac{\partial \overline{(p'w')_s}}{\partial z} = \frac{1}{\rho} \frac{\partial D_{sf}}{\partial z} c_s. \quad (19)$$

Integration of this equation from the surface up to a height z yields

$$(D_{sf})_0 = \frac{\rho C}{c_s}\left(7.5z - \frac{1}{2}z^2\right) + \text{const.} \qquad (20)$$

Requiring $D_{sf} = 0$ for $z = 7.5$ m gives the surface value of the form drag:

$$(D_{sf})_0 = \text{const.} = -\frac{\rho}{c_s}28C. \qquad (21)$$

With the aid of the concept of wavelength-dependent height of influence, it is possible to roughly identify the maximum wavelength that contributes to the form drag of the short waves. In terms of critical height theory, the basic requirement is that the height $z_{cr} < z_{U\max}$, where $z_{U\max}$ is the height to the wind maximum or knee. If we further assume that $z_w \approx z_{cr}$, this gives a corresponding maximum wave phase speed $c_{\max} = U_{\max}$. Assuming the deep-water relation

$$c = \sqrt{\frac{g\lambda}{2\pi}}, \qquad (22)$$

we obtain the corresponding wavelength

$$\lambda_{\max} = \frac{2\pi}{g}U_{\max}^2 \qquad (23)$$

and the corresponding frequency

$$n_{\min} = \frac{U_{\max}}{\lambda_{\max}}. \qquad (24)$$

Table 1 lists derived values for $n_{\min}$, $\lambda_{\max}$, and $U_{\max} = c_{\max}$ for the five swell cases. When determining $(D_{sf})_0$ with Eq. (21), c_s is arbitrarily set equal to $c_{\max}$, which means that the value obtained for $(D_{sf})_0$ represents the lower bound (because $c_s \leq c_{\max}$).

Figures 3a–f show mean 1D wave spectra from the ASIS buoy for the five swell cases and the growing sea case, respectively. For cases C1 and F1 (Figs. 3a,b) there is little energy above $n_{\min} = 1.1$ Hz, which, in accordance with the above reasoning, would create a negative form drag. This is in agreement with our interpretation of the T_p curves for these two cases as being simply due to positive form drag from the swell waves. Figures 3c, 3d, and 3e, on the other hand, show that the respective spectra for cases C2, C3, and F2 indeed have energy for $n \geq n_{\min}$ (which value is indicated in each of the plots).

Using the defining equation for the critical height, Eq. (6) gives $z_{cr} = 0.3$ m for the growing sea case, in stark contrast to what is obtained for the swell cases (this being true in an order of magnitude sense also for the more loosely defined term height of influence, z_w). This is in agreement with the finding (Fig. 2f) that $T_p \approx 0$ at all heights for this case.

TABLE 1. Frequencies $n_{\min}$ in wave spectra corresponding to approximate height of influence of short waves for the five swell cases; $\lambda_{\max}$ is the corresponding wavelength and $U_{\max}$ the wind speed at the maximum or knee = $c_{\max}$.

Case	$n_{\min}$ (Hz)	$\lambda_{\max}$ (m)	$U_{\max}$ (m s^{-1})
C1	1.1	1.2	1.4
F1	1.0	1.6	1.6
C2	0.39	10	4.0
C3	0.35	13	4.5
F2	0.29	18	5.4

Table 2 lists measured total stress $\rho u_{*_0}^2$; the form drag of swell waves $(D_p)_0$ and short waves $(D_{sf})_0$, respectively; the viscous stress, D_{visc} [derived as a residual from Eq. (17)]; and the ratios of $(D_p)_0$ and $(D_{sf})_0$ to $\rho u_{*_0}^2 + (D_p)_0$. For young seas,

$$(D_{sf})_0/[\rho u_{*_0}^2 + (D_p)_0] = \frac{(D_{sf})_0}{\rho u_{*_0}^2} = -\alpha_c, \qquad (25)$$

where α_c is the coupling parameter, which shows how much of the total stress at the surface is supported by the form drag. Makin and Kudryavtsev (1999, their Fig. 4.11) present simulations and laboratory data by Banner and Peirson (1996), which indicate clearly that α_c is strongly wind speed dependent, with values in the range 0.2–0.3 for $U_{10} = 4$ m s^{-1}. Direct comparison with our measurements for cases that include contributions from swell is not straightforward, so we add $(D_p)_0$ to $\rho u_{*_0}^2$ in the denominator. For cases C2, C3, and F2, $(D_{sf})_0/[\rho u_{*_0}^2 + (D_p)_0]$ is found to be in the range 17%–56%, which is in reasonable agreement with the results of Makin and Kudryavtsev (1999), particularly considering that $(D_p)_0$ and $(D_{sf})_0$ are expected to have the same degree of uncertainty as T_p, typically $\pm 50\%$. An important uncertainty in the determination of $(D_{sf})_0$ comes from arbitrarily setting $c_s = c_{\max}$ as noted above.

The corresponding ratio for the form stress from swell, $(D_p)_0/[\rho u_{*_0}^2 + (D_p)_0]$ is in the range of 15%–27% for cases C2, C3, and F2. This should be compared with corresponding values reported by Sullivan et al. (2000, their Fig. 10) from direct numerical simulations, which shows the form drag to be $< \sim 5\%$ of the total stress for $c/u_* > \sim 15$ (i.e., for swell waves). This must be regarded as close enough considering the expected degree of uncertainty of our data ($\pm 50\%$, as reported above).

e. Deriving a hypothetical nonswell wind profile by removing the pressure transport term

Neglecting the left-hand side terms of Eq. (7), the wind gradient $\partial U/\partial z$ can be expressed in terms of the TKE budget by dividing through with $\overline{u'w'}$:
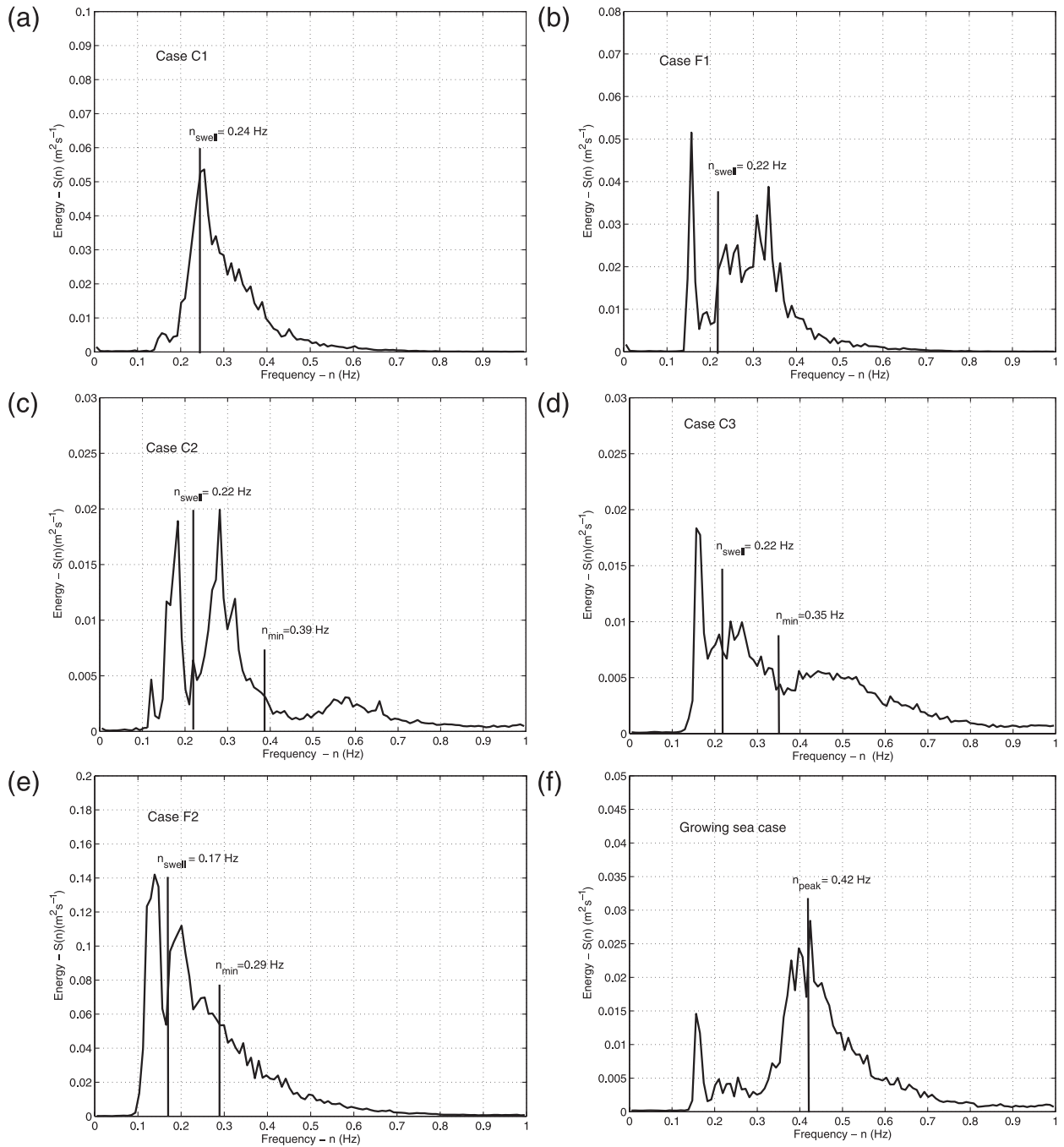
FIG. 3. Mean 1D wave spectra for different cases, measured at the ASIS buoy; n_{swell} is the frequency used in the calculations in the text. Cases (a) C1; (b) F1; (c) C2; (d) C3; (e) F2; and (f) for the growing sea case. In (c)–(e), n_{min} indicates the lower frequency limit for contributions to the nonswell form drag.

$$\frac{\partial U}{\partial z} = -\frac{1}{\overline{u'w'}}\left(-\frac{g}{T}\overline{w'\theta_v'} + \frac{\partial}{\partial z}\frac{\overline{w'q'^2}}{2} + T_p + \varepsilon\right). \quad (26)$$

For cases C2, C3, and F2, integration of Eq. (26) from the ground to height z should, by definition, give the observed wind profile for this height interval (this procedure is not

possible for cases C1 and F1 for which $\overline{u'w'} = 0$). The effect of the pressure transport term on the wind profile can be obtained by isolating the corresponding term from (26):

$$\left(\frac{\partial U}{\partial z}\right)_{T_p} = -\frac{T_p}{\overline{u'w'}}. \quad (27)$$

TABLE 2. Measured total stress, $\rho u_{*_0}^2$ (kg s^{-2} m^{-1}); estimated form stress from swell waves, $(D_p)_0$, and from short waves, $(D_{sf})_0$; and estimated viscous stress, D_{visc}. Last two columns give ratios of $(D_p)_0$ and $(D_{sf})_0$ to $\rho u_{*_0}^2 + (D_p)_0$.

Case	$\rho u_{*_0}^2 \times 10^3$	$(D_p)_0 \times 10^3$	$(D_{sf})_0 \times 10^3$	$D_{visc} \times 10^3$	$\dfrac{(D_p)_0}{\rho u_{*_0}^2 + (D_p)_0} \times 100$	$\dfrac{(D_{sf})_0}{\rho u_{*_0}^2 + (D_p)_0} \times 100$
C1	0.0	1.3	0	−1.3	100	0
F1	0.0	0.5	0	−0.5	100	0
C2	11.1	4.2	−8.6	−6.7	27	−56
C3	23.4	5.6	−11.0	−18.0	19	−38
F2	43.1	7.7	−8.7	−42.0	15	−17

Integrating Eq. (27) from the lowest measuring point 2.56 m to a height z,

$$U(z) - U(2.5m) = \int_{2.5m}^{z} \frac{T_p}{u_*^2}\, dz, \qquad (28)$$

gives the contribution from the pressure transport term to the observed wind profile. To reduce scatter, T_p was taken from the empirically derived expressions for the sum of the exponential and the linear expression below 7.5 m for each case and as the exponential expression for $z > 7.5$ m; also, $\overline{u'w'}$ was taken from the measurements for the heights 2.56, 5.3, 10, 18, and 26 m (Fig. 9 in SH09). Linear interpolation of $T_p/\overline{u'w'}$ enabled evaluation of second-order polynomials of $\Delta U(z)$ for each of the five height intervals.

In Fig. 4 the original, measured wind profile (curve with circles) and the corresponding wind profile obtained after subtracting the contribution from Eq. (28) (curve with triangles) is shown for one case, F2. The figure illustrates how the characteristic knee feature in the original swell profile completely disappears when the pressure transport effect is removed. A similar result is obtained for cases C2 and C3 as well (not shown), which both have modified wind profiles with wind gradients that decrease monotonically with height.

5. Discussion

Studies over the sea with simultaneous measurements at several levels from 2.5 to 30 m are rare. In fact, many measurements start at around 10 m. This means that the wind speed maximum or knee at 5–10 m is not observed. This was the case with previous measurements during swell at Östergarnsholm (e.g., Smedman et al. 1999). In that case it was noted that the wind gradient above 8 m was slightly negative, indicating that a wind maximum must be present at some lower height; T_p was calculated as a residual term of the TKE budget (in a similar manner to what was done here) and at 10-m height this term was observed to be negative and of the same order of magnitude as in the present study. Similar

observations were made in other studies based on measurements from the same site (Rutgersson et al. 2001; Sjöblom and Smedman 2002, 2003). Based on an analogy with the findings from a previous study at another site in the Baltic Sea (Smedman et al. 1994), these authors suggested the observed pressure transport at 10 m to be a result of inactive turbulence being transported down toward the surface from a strong shear zone at the top of the boundary layer and not upward from the swell waves.

The T_p curve of Smedman et al. (1994) was obtained as a combination of measurements on a tower and from an instrumented aircraft. The plot, reproduced here (with an addition of possible extrapolations) as Fig. 5, shows a rapid decrease of $-T_p$ with height from the surface up to a height of around $0.3z_i$ (where z_i is the height of the boundary layer), at which point it starts increasing with height to a maximum around $0.6z_i$, which is the height of maximum wind shear. In light of the present study, it is natural to interpret this curve as the sum of two contributions—as indicated with possible extrapolations in Fig. 5—one derived from the elevated wind maximum and the other from the form drag of the swell waves. In the present study we see no sign of a contribution from higher levels; rather, the graphs (Figs. 2a–e) give an impression of asymptotic decrease with height toward zero.

The present measurements were made in the Baltic Sea, with unidirectional swell of fairly small amplitude and slope factor (Table 1 of SH09). Typical swell waves over the World Ocean may be multidirectional and have much larger amplitude. The present study does not give any information on how changes in these parameters may affect the outcome. In SH09 comparisons were made with results from the large-eddy simulations of Sullivan et al. (2008). The simulated swell waves have a significant wave height of 4 m, compared with 0.2–0.6 m in our case, and a wave slope factor of 0.1 as compared with 0.015–0.03 in our case. Nevertheless, the LES for the case with wind-following swell and slight convection agrees qualitatively well with our results.

Thus, it appears possible that the atmospheric effects from the wave field are rather robust, in the sense that as long as there is a well-defined swell peak in the wave
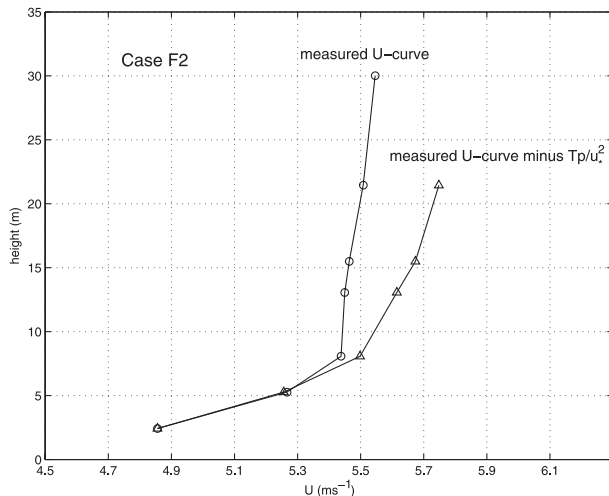
FIG. 4. Original wind profile for case F2 (curve with open circles) and the corresponding profile obtained after subtraction of the contribution from the pressure transport term (curve with triangles).

FIG. 5. Reanalysis of airborne and tower measurements of Smedman et al. (1994). Measured TKE imbalance term (solid line on right), imbalance interpreted as pressure transport (crosses and circle), wind profile (solid line on left), time rate of change of TKE (curve with triangles). Thin dashed lines indicate possible extensions of two separate curves that could make up the net imbalance; z_i is depth of the boundary layer, 1200 m.

spectrum, the characteristic effects on the boundary layer structure that we observe in this study—a low-level wind maximum or knee and nonvalidity of Monin–Obukhov similarity—seem not very sensitive to the details of the wave spectrum. Thus, for example, the observed atmospheric characteristics for cases C1 and F1 are very close, which contrasts strongly to the very dissimilar wave spectra (Figs. 3a and 3b, respectively). Also, cases C2, C3, and F2 have strong similarities in wind profile shape and TKE budget details, but the corresponding wave spectra (Figs. 3c, 3d, and 3e, respectively) vary considerably in their details. For these characteristic atmospheric features to occur, however, the swell component must dominate energetically over corresponding contributions from shorter waves. Thus, the growing sea case wave spectrum (Fig. 3f) has a pronounced young sea maximum for $n \approx 0.4$ Hz but also an additional small swell peak at $n \approx 0.17$ Hz. The corresponding TKE budget (Fig. 2f) has $T_p \approx 0$ at all heights and wind increasing monotonically with height, showing no evidence of swell effects. This is consistent with Drennan et al. (2005), who found nondominant swell waves to have little impact on effective sea surface roughness and air–sea momentum exchange.

6. Conclusions

All terms of the turbulence kinetic energy budget except the pressure transport term, T_p, but including the local time rate of change of TKE and the horizontal advection term, could be determined directly from measurements for five cases with dominant swell and

one reference case with growing sea. This enabled reasonably accurate estimates of the pressure transport term T_p to be made. It was demonstrated that for two cases with $c_p/U_8 \approx 5$, this term is a gain, the magnitude of which decreases asymptotically to zero at great heights. Analytically, this decrease is well described by $e^{-1.9kz}$, where k is the wavenumber of the dominant swell waves, a result that is in agreement with published results from large-eddy simulations of atmospheric flow over monochromatic swell waves. For three cases with c_p/U_8 in the approximate range 1.5–2, T_p decreases similarly above about 10 m but is positive (i.e., a loss) at lower heights. This was interpreted as signatures of shorter waves riding on top of the swell. Thus, the observed T_p curve for these cases was treated as the sum of a negative, exponentially decaying function, caused by a positive form drag from the swell waves and a contribution of opposite sign decreasing approximately linearly with height for $z < 10$ m, which is produced by negative form drag.

By integration of the observed exponential and linear curves for T_p, it was possible to derive approximate estimates of the form drag at the surface from swell and shorter waves, respectively. The ratio of these contributions to the sum of observed shearing stress and swell form stress at the surface compare favorably with results from previous studies.

A reference wind-sea case, with wind speed and stability similar to one of the swell cases but with $c_p/U_8 = 0.63$, shows $T_p \approx 0$ at all heights.

The mean wind gradient $\partial U/\partial z$ can be expressed as the negative of the sum of the buoyancy term, the turbulent transport term, the pressure transport term, and the dissipation term divided by $\overline{u'w'}$ [Eq. (26)]. Thus, by subtracting the term $T_p/\overline{u'w'}$ and integrating with respect to the height z, it was possible to study the influence of this term on the mean wind profile for three swell cases with $\overline{u'w'} \neq 0$. This procedure produces a wind profile that increases monotonically with height, thus strongly suggesting that the observed feature found for these cases of a knee in the swell wind profiles is caused by the pressure transport term. The two cases with a clear wind maximum around 6–8 m above the water surface could not be subjected to this test because there $\overline{u'w'} \approx 0$.

The findings from this study cannot simply be used to extrapolate to results more typical of oceanic conditions with larger wave heights and multicomponent swells, but the results appear to be fairly robust with regard to the details of the wave field, the important issue being the presence of a pronounced swell peak in the wave spectrum. The characteristic atmospheric features that ensue are (i) a wind profile with either (for relatively large c_p/U_8) a wind maximum at low height—in this case 5–10 m—or a distinct knee structure (i.e., rapidly increasing wind below this same height and approximately constant wind above); (ii) nonvalidity of Monin–Obukhov similarity theory; (iii) more or less strongly reduced shearing stress at the surface, sometimes even positive net stress (i.e., the swell waves deliver momentum to the airflow); and (iv) the effect of the swell waves on the atmospheric boundary layer (ABL) being global, as noted by Sullivan et al. (2008) (i.e., it may extend throughout the ABL). From the present study it appears also that the atmospheric response is rather insensitive to the wind–swell angle within $\pm 90°$—a result that (as shown in SH09) is expected from the wind flow geometry over the swell waves in a coordinate system moving with the wave system.

APPENDIX

Evaluation of Mean Values of Each Term of the TKE Budget and of Corresponding Error Estimates

a. The production term, P

For the tower levels, the following expression was used:

$$P(z_j) = \overline{u'w'}(z_j)\frac{U(z_{j+1}) - U(z_{j-1})}{z_{j+1} - z_{j-1}}, \qquad \text{(A1)}$$

where z_j denotes one of the three turbulence levels and z_{j+1} and z_{j-1} are the anemometer levels closest above and below the turbulence level z_j; $\overline{u'w'}(z_j)$ was evaluated in section 2d of SH09 and shown in Fig. 9 of that paper.

Near the surface the wind speed varies rapidly with height, and the above method is not satisfactory. For cases C2, C3, and F2, the reasonable hypothesis is made that close to the surface the wind profile converges to the logarithmic form, which can be written in dimensionless form:

$$\varphi_m = \frac{\kappa z}{u_*}\frac{\partial U}{\partial z} = 1, \quad \text{for} \quad z \to 0, \qquad \text{(A2)}$$

where κ is the van Karman constant $= 0.40$ and $u_* = \sqrt{-(\overline{u'w'})_0}$. For $z = 5.3$ m, φ_m can be evaluated with an interpolation formula similar to (A1):

$$(\varphi_m)_{5.3m} = \frac{\kappa 5.3}{\sqrt{(-\overline{u'w'})_{5.3}}}\frac{U_{8.1} - U_{2.4}}{8.1 - 2.4}. \qquad \text{(A3)}$$

It is further assumed that φ_m varies linearly from unity at the surface to the value derived with (A3) at 5.3 m. From this relation, φ_m at 2.56 m can be derived and hence

$$P_{2.56} = \frac{u_*^3}{\kappa 2.56}(\varphi_m)_{2.56}, \qquad \text{(A4)}$$

where $u_* = \sqrt{-(\overline{u'w'})_{2.56}}$. In a corresponding way, $P_{5.3}$ is obtained from an expression formally similar to Eq. (A4), but with $(\varphi_m)_{5.3m}$ taken from Eq. (A3) and $u_* = \sqrt{-(\overline{u'w'})_{5.3}}$ and, of course, with 5.3 instead of 2.56 in the denominator. Estimates of P were evaluated for each individual half hour. For cases C1 and F1, $u_* = 0$, and P is zero at all heights.

ERROR ANALYSIS FOR THE TERM P

The net error in P [cf. Eq. (A1)] results from a combined uncertainty in $\overline{u'w'}$ due to the finite sampling effect, (s.e.m.)P, and a systematic component, δP, and

from the measuring accuracy in $U(z_{j+1})$ and in $U(z_{j-1})$, δU. Here

$$(\text{s.e.m.})P = \frac{\sigma_P}{\sqrt{N}}, \qquad (A5)$$

where σ_P = standard deviation of the N 30-min means that make up a case.

The systematic component δP results from inaccurate performance of the individual sonic instruments. From plots of vertical profiles of $\overline{u'w'}$ and from an instrument intercomparison study [see Högström and Smedman (2004), in which sonic anemometers were compared in the field with the very accurate Uppsala University Meteorology Group (MIUU) instrument], it was concluded that this term can be given as $\delta P \approx 0.07P$.

The error in wind speed $\delta U \approx 0.05$ m s^{-1}, so the error in $\Delta U \approx 0.07$ m s^{-1} and the corresponding error in P is

$$\delta P_U \approx \frac{P}{\Delta U} \delta U \approx \frac{0.07}{\Delta U} P. \qquad (A6)$$

Thus, the combined error in P is obtained from

$$\delta P \approx \sqrt{[(\text{s.e.m.})P]^2 + (0.07P)^2 + \left(\frac{0.07P}{\Delta U}\right)^2}. \quad (A7)$$

Here, the last term under the square root sign is much smaller than the other two terms (note that 0.07 in this term is in m s^{-1}).

b. The buoyancy production term

The buoyancy term

$$B = -g/T \, \overline{w'\theta'_v}.$$

As shown in Table 1 of SH09, $\overline{w'\theta'_v}$ ranges from about 1.7×10^{-3} m s^{-1} K for cases C1 and F1 to 21×10^{-3} m s^{-1} K for case F2. The standard error of the mean B for each height and case was evaluated and plotted as error bars in the TKE plots. Note that although the B curves may vary to some extent with height, it is not possible to discern any systematic pattern.

c. The turbulent transport of TKE, T_t

$$T_t = \frac{1}{2} \frac{\partial}{\partial z} \left(\overline{w'u'^2} + \overline{w'v'^2} + \overline{w'^3} \right) = \frac{\partial \overline{w'E'}}{\partial z}. \quad (10)$$

Thus, each of the third-order moments $\overline{w'u'^2}$, $\overline{w'v'^2}$, and $\overline{w'^3}$ must be evaluated and summed at each of the five turbulence levels. Then regression curves must be determined from which, in turn, the required derivative will be extracted. Third-order turbulence moments require, however, very long time averaging to converge to their en-
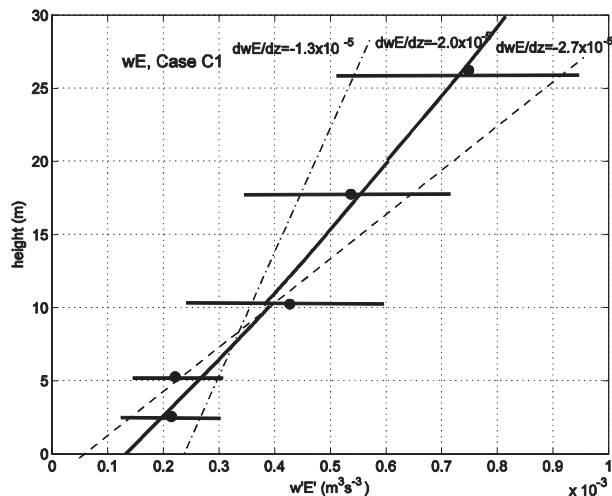
FIG. A1. The quantity $\overline{w'E'}$ plotted as a function of height for case C1. Filled circles are mean values; horizontal bars ±standard error of the mean. Three straight lines have been drawn to represent, respectively, a mean and a likely range of fits. Corresponding values for the slope are given.

semble averages (cf., e.g., Monin and Yaglom 1971). Thus, due account must be taken of the statistical uncertainty. Figure A1 illustrates the procedure. The quantity $\overline{w'E'}$ has been plotted for case C1 as a function of height. Calculated mean values are shown as filled circles. Also shown, as error bars, is the standard error of the mean, s.e.m. = $\sigma/\sqrt{N}$, where σ is the standard deviation and N the number of half-hour periods for each case (here $N = 10$).

It is obvious from the figure that the uncertainty of every estimate of the mean is great. Requiring a best-fit curve to pass between the limits of ±s.e.m. for each level indicates that for this particular case, a linear fit is a reasonable approximation. The three lines drawn in the figure have the respective slopes of -1.3×10^{-5}, -2.0×10^{-5}, and -2.7×10^{-5} m s^{-3}. Thus, for case C1, $T_t = $ const $= -2.0 \times 10^{-5} \pm 0.7 \times 10^{-5}$ m^2 s^{-3}.

Similar procedures have been adopted for each of the six cases (five swell cases and one growing sea case). Only cases C1 and F1 give a straight-line best fit for $\overline{wE}(z)$, with the remaining cases having curves with significantly greater slope near the surface than higher up (not shown). The expected relative uncertainty in the estimates of T_t is, however, similar to that shown above for case C1. In the TKE plots, the estimates of ±s.e.m. for T_t is indicated with error bars.

d. The dissipation term, ε

Invoking Taylor's hypothesis, ε can be derived from inertial subrange u component spectra:

$$\varepsilon = \frac{2\pi n}{U} \left[\frac{nS_u(n)}{\alpha_1} \right]^{3/2}. \qquad (12)$$

Here α_1 is a universal constant ≈ 0.50 (cf. Högström 1990 and the text below) and n must be chosen in the region with $-\frac{2}{3}$ slope.

Many of the u spectra have upward-turning high-frequency tails (an effect of electronic noise, particularly evident for low wind speed), this being particularly evident in the measurements from the two ASIS levels, but also, to a lesser extent, in the spectra from 18 and 26 m. The 10-m spectra are, however, virtually free from this kind of problem, experiencing a clean $-\frac{2}{3}$ regime for most of the frequency range 0.2 Hz $< n <$ 9 Hz.

For each of the six cases (five swell cases and one reference growing sea case), mean spectra for all five levels were plotted together in log–log representation (not shown). For cases C2, C3, and F2 the upward-turning high-frequency tails usually start at a frequency above 1 Hz, and it was considered reasonable to draw lines with $-\frac{2}{3}$ slope parallel to the corresponding 10-m curve in each plot. For cases C1 and F1, the spectral levels rise rapidly around 0.1 Hz for the two ASIS levels; for the spectral range 0.1 $< n <$ 1 Hz the corresponding spectra experience large scatter, but a lower level with reasonable $-\frac{2}{3}$ slope can be identified.

ERROR ANALYSIS FOR THE TERM ε

The uncertainty in the estimates of dissipation derives from several possible sources, which will each be considered separately and together to form a net error $\delta\varepsilon$:

$$\delta\varepsilon = \overline{\varepsilon}\sqrt{\left(\frac{3}{2}\frac{\delta\alpha_1}{\alpha_1}\right)^2 + \left(\frac{\delta U}{U}\right)^2 + \left\{\frac{3}{2}\frac{\delta[nS_u(n)]}{nS_u(n)}\right\}_1^2 + \left\{\frac{3}{2}\frac{\delta[nS_u(n)]}{nS_u(n)}\right\}_2^2}. \quad (A8)$$

The uncertainty in the Kolmogoroff parameter α_1: According to Table 1 of Högström (1990), which lists results from 20 datasets, the best estimate after correction for fluctuation convective velocity is 0.50, with s.e.m. 0.03, that is, $\delta\alpha_1/\alpha_1 \approx 0.06$. As noted above (in the analysis of the error in P), $\delta U \approx 0.05$ m s^{-1}. The third term under the square root sign is due to the variation of the values for the individual 30-min mean spectra within a case.

The last term under the square root sign is an attempt to evaluate the effect due to inadequate adaption to true inertial subrange conditions. Thus, the ratio $nS_w(n)/nS_u(n)$ is predicted to equal $\frac{4}{3}$ in the inertial subrange. Actual values for $z = 10$ m scatter around 1.3 for cases C2, C3, and F2 in the frequency range 1 $< n <$ 9 Hz. For cases C1 and F1, there is a reasonably well-defined $-\frac{2}{3}$ slope in the u spectrum for this level in the frequency range $10^{-2} < n < 1$ Hz (and a high-frequency tail for $1 < n < 9$ Hz) but a nonmonotonic curve shape in the corresponding w spectrum, indicating that a final $-\frac{2}{3}$ region has not been reached for $nS_w(n)$ for $n < 1$ Hz. It is, however, reasonable to conclude that the level of the long $-\frac{2}{3}$ slope of $nS_u(n)$ is likely to give an acceptable estimate of ε for C1 and F1 as well. The spectral ratio has only been evaluated for the 10-m level because of the upward-turning high-frequency tails encountered frequently in the spectra for the other levels (which are due to electronic noise). Nevertheless, it seems a reasonable conclusion that, in an average sense, unbiased estimates of ε are likely obtained from evaluation of the $-\frac{2}{3}$ regions of the u spectra at all heights and for all cases. However, the fourth term in Eq. (A8) takes into account the observed deviation in the $nS_w(n)/nS_u(n)$ ratio from the ideal value of $\frac{4}{3}$. Thus, with the value of the observed spectral ratio $= k$, the last term is assumed to be $[\frac{3}{2}(k - 1.33)/1.33]^2$.

e. Left-hand-side terms of the TKE budget, Eq. (7)

1) THE TIME RATE OF CHANGE TERM, TRC

$$\text{Trc} = \frac{\partial \overline{q'^2}}{2\partial t} = \frac{1}{2}\frac{\partial}{\partial t}(\overline{u'^2} + \overline{v'^2} + \overline{w'^2}). \quad (A9)$$

This term was first evaluated for the 10-m height for all five swell cases and the growing sea case by linear regression of the trend in $\overline{q'^2}/2$ from the series of consecutive 30-min means. For cases like C1, which consists of two periods widely separated in time, separate regression was performed for each subperiod, and the mean slope for the two periods was chosen to represent the case. Table A1 gives derived values of $\partial\overline{E}/\partial t = \delta_{10}$ for 10 m (where $E = \overline{q'^2}/2$). All values are on the order of 10^{-6} m^2 s^{-3}. As seen in the main text, the derived value for T_p at 10 m is of particular interest in the analysis of the TKE results. Because of this, the ratio δ_{10}/T_{p10} is also given in Table A1. For cases C2, C3, and F2 this quantity is very small; for cases C1 and F1 it is 0.11 and 0.18 respectively, which is, however, also small considering the uncertainty of T_{p10}. Also given in Table A1 are the Trc term for 2.5, 5, 18, and 26 m for cases C1 and F1, showing that this term is of similar magnitude at all heights.

2) THE ADVECTION TERM, ADV, OF EQ. (7)

This term was evaluated from the simultaneous measurements at the Östergarnsholm tower and ASIS, so the advection term becomes

TABLE A1. Estimates of the time rate of change term of TKE, $\partial E/\partial t_{10} = \delta_{10}$, for 10 m, and the advection term of TKE by the mean wind, Adv $= U_x \partial U/\partial x$. Also given is the magnitude of the pressure transport term T_p at 10 m and the ratio of $\delta = \delta_{10}$ and $A =$ Adv to $T_p = T_{p10}$. Finally, $\partial E/\partial t_{2.5} = \delta_{2.5}$ and the corresponding terms for 5, 18, and 26 m are given for cases C1 and F1.

Case	$10^6 \delta_{10}$	$10^4 \overline{T}_{p10}$	δ/T_p	10^6Adv	A/T_p	$10^6 \delta_{2.5}$	$10^6 \delta_5$	$10^6 \delta_{18}$	$10^6 \delta_{26}$
C1	4.5	−0.4	−0.11	−6.0	0.15	−1.0	−1.3	4.1	3.8
F1	−4.4	−0.25	0.18	−1.8	0.007	−3.3	−3.5	−4.4	−4.5
C2	4.0	−3.0	−0.01	−6.0	0.02	—	—	—	—
C3	1.1	−3.0	−0.004	−0.045	0.0002	—	—	—	—
F2	8.0	−10	−0.008	0.19	0.0002	—	—	—	—
Grsea	7.0	—	—	38	—	—	—	—	—

$$\mathbf{U} \cdot \mathbf{\nabla} \frac{\overline{q'^2}}{2} \approx \overline{U_8 \cos(\varphi - 110°)(E_{\text{tower}} - E_{\text{ASIS}})}/4000,$$
$$(\text{A10})$$

where U_8 is the wind speed at 8 m; the connection line between the two sites is roughly 4000 m long and oriented along 110°; ϕ is the wind direction; E_{tower} is the measured TKE at 10 m on the tower; and $E_{\text{ASIS}} = E_5 + a$, where a is a correction for the mean variation of E from 5 to 10 m, obtained from profile plots of $\overline{E}(z)$. As seen from Table A1, the advection term is of the same order of magnitude as the time rate of change term or smaller. For case C1 it is 15% of T_{p10}, but for the other cases it is less than 3%. Note that for this case the two imbalance terms Trc and Adv are of similar magnitude but of different sign, so that their sum divided by T_{p10} is just 0.04.

In conclusion, both the left-hand-side terms of Eq. (7) are of insignificant magnitude for all cases. For cases C2, C3, F2, and "growing sea," the magnitude is so small that they could not be distinguished from the zero line if plotted in the corresponding TKE graphs, Figs. 2c–f. For cases C1 and F1 the two terms could just barely be distinguished if they were included in Figs. 2a,b. But for the sake of clarity they have not been included in these plots, as their magnitude is small compared to the uncertainty of the other terms.

REFERENCES

Banner, M. L., and W. L. Peirson, 1996: Tangential stress beneath wind-driven air–water interfaces. *J. Fluid Mech.,* **364,** 115–145.

Donelan, M. A., A. V. Babanin, I. R. Young, and M. L. Banner, 2006: Wave-follower field measurements of the wind-input spectral function. Part II: Parameterization of the wind input. *J. Phys. Oceanogr.,* **36,** 1672–1689.

Drennan, W. M., P. K. Taylor, and M. J. Yelland, 2005: Parameterizing the sea surface roughness. *J. Phys. Oceanogr.,* **35,** 835–848.

Elliott, J. A., 1972: Instrumentation for measuring static pressure fluctuations within the atmospheric boundary layer. *Bound.-Layer Meteor.,* **2,** 476–495.

Graber, H. C., E. A. Terray, M. A. Donelan, W. M. Drennan, J. C. Van Leer, and D. B. Peters, 2000: ASIS—A new air–sea interaction spar buoy: Design and performance at sea. *J. Atmos. Oceanic Technol.,* **17,** 708–720.

Grachev, A. A., and C. W. Fairall, 2001: Upward momentum transfer in the marine boundary layer. *J. Phys. Oceanogr.,* **31,** 1698–1711.

Hanley, K. E., and S. E. Belcher, 2008: Wave-driven wind jets in the marine atmospheric boundary layer. *J. Atmos. Sci.,* **65,** 2646–2660.

Högström, U., 1990: Analysis of turbulence structure in the surface layer with a modified similarity formulation for near neutral conditions. *J. Atmos. Sci.,* **47,** 1949–1972.

——, and A.-S. Smedman, 2004: Accuracy of sonic anemometers: Laminar wind-tunnel calibrations compared to atmospheric in situ calibration against a reference instrument. *Bound.-Layer Meteor.,* **111,** 33–54.

——, and Coauthors, 2008: Momentum fluxes and wind gradients in the marine boundary layer: A multi-platform study. *Boreal Environ. Res.,* **13,** 475–502.

Hristov, T. S., C. Friehe, and S. D. Miller, 1998: Wave-coherent fields in air flow over waves: Identification of cooperative behavior buried in turbulence. *Phys. Rev. Lett.,* **81,** 5245–5248.

——, S. D. Miller, and C. A. Friehe, 2003: Dynamical coupling of wind and ocean waves through wave-induced air flow. *Nature,* **422,** 55–58.

Kolmogoroff, A. N., 1941: Local structure of turbulence in an incompressible viscous fluid at very high Reynolds numbers. *Dokl. Akad. Nauk SSSR,* **30,** 299–303.

Makin, V. K., and V. N. Kudryavtsev, 1999: Dynamical coupling of surface waves with the atmosphere. *Air–Sea Exchange: Physics, Chemistry and Dynamics,* G. L. Geernaert, Ed., Kluwer Academic, 73–125.

Miles, J. W., 1957: On the generation of surface waves by shear flows. *J. Fluid Mech.,* **3,** 185–204.

Monin, A. S., and A. M. Yaglom, 1971: *Statistical Fluid Mechanics: Mechanics of Turbulence.* Vol. 1. MIT Press, 769 pp.

Pettersson, H., H. C. Graber, D. Hauser, C. Quentin, K. K. Kahma, W. M. Drennan, and M. A. Donelan, 2003: Directional wave measurements from three wave sensors during the FETCH experiment. *J. Geophys. Res.,* **108,** 8061, doi:10.1029/2001JC001164.

Rutgersson, A., A.-S. Smedman, and U. Högström, 2001: Use of conventional stability parameters during swell. *J. Geophys. Res.,* **106,** 27 117–27 134.

Sjöblom, A., and A.-S. Smedman, 2002: The turbulent kinetic energy budget in the marine atmospheric surface layer. *J. Geophys. Res.,* **107,** 3142, doi:10.1029/2001JC001016.

——, and ——, 2003: Vertical structure in the marine atmospheric boundary layer and its implication for the inertial dissipation method. *Bound.-Layer Meteor.,* **109,** 1–25.

Smedman, A.-S., M. Tjernström, and U. Högström, 1994: The near-neutral marine atmospheric boundary layer with no shearing stress: A case study. *J. Atmos. Sci.,* **51,** 3399–3411.

——, U. Högström, H. Bergström, A. Rutgersson, K. K. Kahma, and H. Pettersson, 1999: A case study of air–sea interaction during swell conditions. *J. Geophys. Res.,* **104,** 25 833–25 851.

——, ——, E. Sahleé, W. M. Drennan, K. K. Kahma, H. Pettersson, and F. Zhang, 2009: Observational study of marine atmospheric boundary layer characteristics during swell. *J. Atmos. Sci.,* **66,** 2747–2763.

Sullivan, P. P., J. C. McWilliams, and C.-H. Moeng, 2000: Simulation of turbulent flow over idealized water waves. *J. Fluid Mech.,* **404,** 47–85.

——, J. B. Edson, J. C. McWilliams, and C.-H. Moeng, 2004: Large-eddy simulations and observations of wave-driven boundary layers. Preprints, *16th Symp. on Boundary Layers and Turbulence,* Portland, ME, Amer. Meteor. Soc., 8.12.

——, ——, T. Hristov, and J. C. McWilliams, 2008: Large-eddy simulations and observations of atmospheric marine boundary layers above nonequilibrium surface waves. *J. Atmos. Sci.,* **65,** 1225–1245.